Title: Liquefaction of the brain following stroke shares a similar molecular and morphological profile with atherosclerosis and mediates secondary neurodegeneration in an osteopontin dependent mechanism

Abbreviated Title: Liquefactive necrosis after stroke and atherosclerosis share an osteopontin dependent mechanism

Amanda Chung*[1], Jennifer Frye*[1], Jacob C. Zbesko[1], Eleni Constantopoulos[2], Megan Hayes[1], Anna G. Figueroa[3], W. Antony Day[4], John P. Konhilas[2], Brian S. McKay[3], Thuy-Vi Nguyen[1,5], and Kristian P. Doyle**[1,5,6]

[1]Department of Immunobiology, University of Arizona, Tucson, Arizona, 85719. USA.

[2]Department of Physiology and Sarver Molecular Cardiovascular Research Program, University of Arizona, Tucson, Arizona, 85724. USA.

[3]Department of Ophthalmology and Vision Science, University of Arizona, Tucson, Arizona, 85719. USA.

[4]Arizona Health Sciences Center Imaging Core Facility, Arizona Research Labs, University of Arizona, Tucson, AZ, 85719. USA.

[5]Department of Neurology, University of Arizona, Tucson, Arizona, 85719. USA.

[6]Arizona Center on Aging, University of Arizona, Tucson, Arizona, 85719. USA.

*Co-first authors that contributed equally to this work

**To whom correspondence should be addressed

Address for correspondence:

Kristian P. Doyle, PhD

Department of Immunobiology

University of Arizona, Tucson

1656 E. Mabel Street

Tucson, Arizona, 85719

Tel: (1) 520-626-7013

Email: doylekr@email.arizona.edu

Abstract

The response to ischemic injury in the brain is different to the response to ischemic injury in other organs and tissues. Almost exclusive to the brain, and for unknown reasons, dead tissue liquefies in response to ischemia by the process of liquefactive necrosis. However, the data we present here indicate that at the macroscopic, microscopic, and molecular level, liquefactive necrosis strongly resembles atherosclerosis. We show that chronic stroke infarcts contain foamy macrophages, cholesterol crystals, high levels of osteopontin and matrix metalloproteinases, and a similar cytokine profile to atherosclerosis. Excessive cholesterol loading of macrophages is a principal driver of atherosclerosis. Therefore, because cholesterol is an important structural component of myelin, liquefactive necrosis in response to stroke may be caused by an inflammatory response to myelin debris that is prolonged by the formation of cholesterol crystals within macrophages. We propose that this results in the chronic production of high levels of proteases, which in a partially osteopontin dependent mechanism, causes secondary neurodegeneration and encephalomalacia of the surrounding tissue. In support of this, we show that genetically ablating osteopontin substantially reduces the production of degradative enzymes following stroke, reduces secondary neurodegeneration, and improves recovery. These findings suggest that treatments that prevent atherosclerosis or target the regression of

atherosclerosis may also be useful for mitigating the harmful effects of liquefactive necrosis following stroke.

Significance Statement (120 words)

Here we provide evidence that chronic stroke infarcts contain cholesterol crystals and provide a potential explanation for why the brain undergoes liquefactive necrosis following ischemia. Specifically, we propose that myelin debris, and cholesterol crystals derived from myelin debris, drive the sustained production of degradative enzymes by macrophages within the infarct for months following stroke. These data suggest that treatments that target cholesterol loading within macrophages, and the sustained production of degradative enzymes, may help to prevent the detrimental effects of brain liquefaction following stroke.

Introduction

In response to ischemia, the brain degenerates by the process of liquefactive necrosis while the heart degenerates by coagulative necrosis (Robbins et al., 2010). Liquefactive necrosis is a chronic inflammatory response that intensifies post-stroke injury (Doyle et al., 2015; Nguyen et al., 2016; Zbesko et al., 2018), persists for months following a stroke, and occurs for unknown reasons. Cholesterol is a central structural component of myelin. This means that in the aftermath of a brain injury the immune system must clear away substantially more cholesterol than in the aftermath of an injury to an alternative area of the body such as the heart following a myocardial infarction. Therefore, the goal of this research was to understand if the brain undergoes liquefactive necrosis in response to stroke due to the high cholesterol content of the brain.

The rationale for this is that in cardiovascular disease, atherosclerotic plaques develop within arteries when macrophages ingest excessive cholesterol in the form of oxidized low-density lipoprotein (LDL) (Moore et al., 2013). Macrophages slowly develop into large proinflammatory foam cells that contain numerous lipid-laden internal cytoplasmic vesicles. Foam cell formation is dictated by the balance between extracellular lipid uptake and reverse lipid transport from the intracellular compartment to extracellular lipid acceptors, such as high-density lipoprotein (HDL). When cholesterol accumulation within a foam cell exceeds the solubility limit of the cell, cholesterol crystals form (Duewell et al., 2010).

Intracellular cholesterol crystals cause both physical damage to organelles by destabilization of the lysosomal compartment, and rupture the plasma membrane (Abela and Aziz, 2005). They can also activate the NLRP3 inflammasome and the Syk and PI3 kinase pathway, resulting in the production of proinflammatory cytokines and degradative enzymes (Duewell et al., 2010; Moore et al., 2013; Corr et al., 2016). In atherosclerosis, intracellular cholesterol crystals perforate cells and nucleate into larger extracellular cholesterol crystals (Moore et al., 2013). These can activate the foreign body response, which also leads to the production of degradative enzymes (Bayliss, 1976; Sheikh et al., 2015). Consequently the goal of this study was to investigate if the overloading of cholesterol by macrophages is not only involved in the formation of atheroma in cardiovascular disease, but due to the fact that the brain is the most cholesterol-rich organ, containing approximately 20% of the body's total cholesterol (Orth and Bellosta, 2012), if it is also a potential explanation for why dead brain tissue undergoes liquefactive necrosis following stroke.

In support of this hypothesis, Cantuti-Castelvetri and colleagues recently demonstrated that in a toxin-induced model of demyelination, myelin debris can overwhelm the efflux capacity of microglia/macrophages, resulting in the formation of cholesterol crystals and a chronic

inflammatory response in aged mice (Cantuti-Castelvetri et al., 2018). Furthermore, transcriptional profiling of macrophages at 7 days after spinal cord injury reveals that they closely resemble foam cells, with lipid catabolism representing their main biological process (Zhu et al., 2017).

Therefore, we used mouse models of myocardial infarction and ischemic stroke to compare the kinetics and characteristics of the inflammatory response to ischemia in the heart, a protein rich organ, to the inflammatory response to ischemia in the brain, a cholesterol rich organ. We then looked-for evidence of overlap in the molecular profile of the chronic inflammatory response to stroke and atherosclerosis. Finally, we tested whether targeting pathways involved in the pathophysiology of atherosclerosis modulate the damaging effects of liquefactive necrosis following stroke.

We show that the brain takes substantially longer than the heart to heal from ischemia, with the induction of a second wave of inflammation that coincides with the formation of intracellular and extracellular cholesterol crystals within the infarct in the weeks following stroke. The second wave notably includes the expression of many of the same pro-inflammatory cytokines associated with atherosclerosis as well as extremely high levels of osteopontin (OPN) and matrix metalloproteinases (MMPs). We then show that the expression of these pro-inflammatory cytokines and proteolytic enzymes is profoundly reduced in OPN deficient mice, and that these animals exhibit an accelerated recovery of motor function and a reduction in secondary neurodegeneration when compared to wildtype (wt) mice. These findings provide a compelling explanation for why the brain liquefies following stroke, that is to say, the processing of myelin debris within macrophages is overwhelmed, leading to the long-term potentiation of proteolytic enzymes. Importantly, they also provide a starting point for testing if treatments that target

atherosclerosis and the chronic production of degradative enzymes are also beneficial for mitigating the damaging effects of liquefactive necrosis in stroke patients.

Materials and Methods

Mice

Adult 10-12-week male C57BL/6 (Stock No: 000664), BALB/c (Stock No: 000651), nucleotide-binding domain and leucine-rich repeat-containing 3$^{-/-}$ (NLRP3$^{-/-}$)(Stock No: 021302), CD36$^{-/-}$ (Stock No: 019006), and osteopontin$^{-/-}$ (OPN$^{-/-}$) (Stock No: 025378) mice were purchased from the Jackson Laboratory. All animals were housed under a 12-hour light/dark schedule with *ad libitum* access to food and water. All experiments were in accordance with protocols approved by the National Institutes of Health guidelines and the University of Arizona Institutional Animal Care and Use Committee.

Stroke surgery

C57BL/6, NLRP3$^{-\backslash-}$, CD36$^{-\backslash-}$, and OPN$^{-\backslash-}$ mice underwent distal middle cerebral artery occlusion (DMCAO) + hypoxia (DH stroke), as described previously (Doyle et al., 2012). Briefly, mice were anesthetized by isoflurane inhalation, core body temperature was maintained at 37ºC, and the skull exposed by creating an incision in the skin and temporalis muscle. The right middle cerebral artery (MCA) was identified and a microdrill was used to penetrate the skull to expose the underlying MCA. The meninges were cut and the vessel cauterized using a small vessel cauterizer (Bovie Medical Corporation). Surgical wounds were closed using Surgi-lock 2oc (Meridian Animal Health). Mice were then immediately transferred to a hypoxia chamber containing 9% oxygen and 91% nitrogen for 45 minutes. Hypoxia increases the size of the infarct and reduces infarct volume variability in C57BL/6 mice (Doyle et al., 2012). Sham surgeries were performed identically to stroke surgeries, except for cauterization of the DMCA.

BALB/c mice underwent DMCAO without hypoxia. BALB/c mice following DMACO have the same size infarct following DMCAO as C57BL/6 mice following DMCAO + hypoxia (Doyle et al., 2012). All mice received one dose of buprenorphine (0.1 mg/kg) via subcutaneous injection immediately prior to surgery. Cefazolin antibiotics (25 mg/kg) and slow-release buprenorphine (1 mg/kg) were subcutaneously administered immediately following surgery.

Myocardial infarction

C57BL/6 mice were placed in the supine position and a light shone onto the neck region for transesophageal illumination to enable the larynx to be visualized through the mouth opening. The tongue was retracted and a guide wire inserted into the trachea. A 20G IV catheter was then laced over the guide wire and advanced into the trachea but not past the trachea bifurcation. The intubation tubing was then connected to a rodent ventilator. A left thoracotomy was then performed by a left lateral incision and transection of the third rib using dissecting scissors. An 8-0 polyethylene suture was threaded underneath the left coronary artery, perpendicular to the long axis of the heart. The ligature was tied and blanching of the myocardium was visually verified. The thoracotomy was then closed in 3 layers: (1) intercostal ribs and muscle, (2) the pectoral muscle, and (3) the skin layers using 7-0 nylon absorbable suture. After each surgery was completed, the expiration line of the ventilator was briefly occluded in order to evacuate the pleural space and establish proper intrapleural pressure. Mice were extubated and recovered on a heating pad. Total time under anesthesia was less than 30 minutes.

Tissue processing

C57BL/6 mice were euthanized at 24 hours, 1 week, 4 weeks, 8 weeks, and 24 weeks after stroke by deep isoflurane anesthesia followed by exsanguination and intracardial perfusion with 0.9% saline. BALB/c, NLRP3$^{-/-}$, CD36$^{-/-}$, and OPN$^{-/-}$ mice were euthanized at 7 weeks following

stroke by the same methods. Brains and hearts were extracted and either snap frozen in liquid nitrogen for biochemical assays, post-immersed in 4% paraformaldehyde (PFA) and transferred to 30% sucrose for cryoprotection for immunohistochemistry processing, or placed in 2.5% glutaraldehyde and 2% PFA for electron microscopy processing. For immunohistochemistry, frozen coronal sections (40 μm or 6 μm) were taken through the entire brain using a Microm HM 450 sliding microtome (Thermo Fisher Scientific).

Immunohistochemistry

Immunostaining was performed on free-floating brain and paraffin embedded heart sections (n=4-6 mice/experimental group) using standard protocols. Primary antibodies against neuronal nuclei (NeuN, 1:500; MilliporeSigma, Cat. No. MAB377, RRID: AB2298772), CD3e (1:1000; BD Biosciences, Cat. No. 550277, RRID: AB393573), CD68 (1:1000; Bio-Rad, Cat. No. MCA1957GA RRID: AB324217), and B220 (1:500; BD Biosciences, Cat. No. 553085, RRID: AB394615) were used in conjunction with the appropriate secondary antibody and ABC Vector Elite (Vector Laboratories) and 3,3'-diaminobenzidine kits (Vector Laboratories) for visualization. Sections were imaged using a digital Keyence BZ-X700 light and fluorescent microscope.

Nissl staining

Brain and heart sections were mounted and hydrated through descending concentrations of ethanol, and subsequently dipped in distilled water. Sections were then immersed in a 0.5% Nissl (Sigma-Aldrich) solution for 1 minute, rinsed in water, differentiated in a 0.25% acetic alcohol solution, and then dehydrated through ascending concentrations of ethanol. Finally, they were defatted in xylene and coverslipped with Entellan (Electron Microscopy Sciences). Sections were imaged using a digital Keyence BZ-X700 light and fluorescent microscope.

Trichrome staining

Trichrome staining was performed on both mounted brain and heart sections (n=3-4 mice/experimental group) to visualize collagen deposition in infarcted tissue. Staining was performed using a trichrome staining kit (abcam, Cat. No. ab150686), following the kit's protocol. Briefly, Bouin's fluid was preheated in a water bath to 56-64ºC and incubated in Bouin's fluid for 1 hour followed by 10 minutes of cooling. Sections were rinsed in tap water for 5 minutes and once in distilled water. Sections were then stained using Weigert's Iron Hematoxylin for 5 minutes and rinsed in running tap water for 2 minutes. Sections were placed in Briebirch Scarlet/Acid Fuchin solution for 15 minutes and subsequently rinsed in water. Sections were then differentiated in Phosphomolybdic/Phosphotungstic acid solution for 10-15 minutes followed by application of Aniline Blue solution for another 5-10 minutes, and finally rinsed in distilled water. Acetic acid solution (1%) was applied to the sections for 3-5 minutes followed by dehydration in 95% ethanol solution, two times in 100% ethanol, defatted in in xylene, and coverslipped with Entellan. Sections were imaged using a digital Keyence BZ-X700 light and fluorescent microscope.

Multiplex immunoassay

Snap-frozen brain and heart tissue samples (n=5-11 mice/experimental group) were sonicated in ice-cold 0.1M PBS containing 1% triton-X and 0.1% sodium deoxycholate, Protease Inhibitor Cocktail (1:100; MilliporeSigma), and Phosphatase Inhibitor Cocktail 2 (1:100; MilliporeSigma). Following centrifugation, 13,000g at 4°C temp for 15 minutes, the total soluble protein concentration of each supernatant was measured using a Direct Detect Infrared Spectrometer (MilliporeSigma). Total MMPs, OPN, and cytokines/chemokines concentrations were then measured using mouse multiplex immunoassay kits with Luminex technology (MilliporeSigma), according to the manufacturer's protocols and recommendations. Each lysate sample, standard, and quality control was measured in duplicate. Plates were read using a MAGPIX instrument (Luminex), and results were analyzed using MILLIPLEX Analyst 5.1 software (MilliporeSigma).

Electron microscopy

Brains (n=3 mice) used for transmission and scanning electron microscopy (EM) were fixed in 2.5% glutaraldehyde + 2% PFA in 0.1 M Pipes buffer for 1 hour at room temperature or overnight at 4°C. Following washes in 0.05 M Pipes buffer/0.05 M glycine and washes in 0.1 M Pipes buffer, dissected stroke regions from each brain were then post-immersed in 1% osmium tetroxide for 1 hour. After fixation, samples underwent washes in deionized water (DIW). Samples for transmission EM were then block stained in 2% aqueous uranyl acetate, washed in DIW, dehydrated through a graded series of ethanols, infiltrated with 1:1 alcohol/Spurr's resin overnight, and embedded in 100% Spurr's resin overnight at 60°C. Samples for scanning EM were dehydrated, incubated in hexamethyldisilazan, and then air dried. Sections for transmission EM were viewed under an FEI Tecnai Spirit microscope (Arizona Health Science Center Core Imaging Facility) operated at 100 kV. Eight-bit TIFF images were captured using an AMT 4 Mpixel camera. Sections for scanning EM were gold coated, and viewed under a FEI Company Inspect S microscope operated at 30 kV.

Cholesterol crystal imaging

Free floating brain sections (n=4-6 mice/experimental group) were washed in 0.1M phosphate buffered saline (PBS) 3 times for 5 minutes each wash. Sections were then mounted and dried on a slide warmer at 40ºC for 1 hour. Sections were then washed 3 times in distilled water for 2 minutes and dried on a slide warmer. Sections were coverslipped using glycerol and the edges of the coverslips were sealed with clear nail polish. Cholesterol crystals in the infarct were then visualized using standard polarized light microscopy using a Keyence BZ-X700 microscope. Images of the infarct that contained cholesterol crystals were captured using a 20x objective. Lipofuscin autofluorescence was captured as an overlay using a TexasRed filter cube to localize the lesion.

Cholesterol crystal isolation and verification

To confirm the presence of cholesterol crystals, sucrose density centrifugation was performed to verify that the crystals we visualized in our tissue have the correct cholesterol crystal density. Stroked mice were euthanized 7 weeks following DH stroke, as described above. The infarcts from C57BL/6 mice (n=5-10) were dissected and pooled. The same was performed with the equivalent area of contralateral cortex from the same mice as a control. The tissue samples were then placed into two sterile 15 mL conical centrifuge tubes containing 750 µL of media (serum-free Neurobasal media, 1× B27 supplement, L-glutamine, and penicillin/streptomycin, without protease/phosphatase inhibitors; Thermo Fisher Scientific). Pooled tissue was then gently triturated by passage through a sterile P1000 pipet. Dissociated cells were centrifuged at 300 rpm for 10 minutes at 4ºC. The supernatant was removed, the pellet was re-suspended in 750 µL of fresh media followed by gentle trituration with a P1000 pipet, and the sample re-centrifuged at 300 rpm for 10 minutes at 4ºC. Again, the supernatant was removed, the pellet was re-suspended in fresh media, and stored at -80ºC. Prior to pouring the sucrose density gradient, infarct samples were spun at 4,000 rpm for 15 minutes at 4ºC. The supernatant was extracted and placed in a 2 mL screw cap micro tube. 1 mL of lysis buffer with added protease and phosphatase inhibitors was added to the pellet and the sample was sonicated in bursts. Following sonication, samples were spun at 13,000 rpm for 15 minutes at 4ºC. The supernatant was extracted and placed in a 2 mL screw cap micro tube and the pellet was resuspended in 200 µL of lysis buffer and triturated. This extraction process was repeated using the equivalent amount of the contralateral cortex. Each sample was poured into a linear sucrose gradient (0-2 M sucrose). Gradients were then centrifuged at 38,000 x g for 3 hours in an ultracentrifuge. Fractions were removed in 200 µL aliquots from the top of the gradient and analyzed for sucrose content with a refractometer. Using polarized microscopy, 10 µL of each fraction was

pipetted onto a slide and the number of cholesterol crystals present in each fraction was counted. This crystal isolation experiment was repeated in three separate experiments.

Quantification of neuronal degeneration

Neurodegeneration in OPN KO mice (n=5-6 per experimental group) was measured by quantifying NeuN in the peri-infarct area. We used NIH Image J analysis software to perform global thresholding in conjunction with a watershed algorithm on both the ipsilateral and equivalent location on the contralateral hemisphere. Fields covering the peri-infarct area were analyzed at bregma 0.02 using a 40X objective. Data is presented as the percent area occupied by NeuN immunoreactivity in the ipsilateral/contralateral hemisphere.

Ladder rung test

Ladder rung testing was performed on wt and $OPN^{-/-}$ mice (n=14 per experimental group) to assess changes in motor recovery following stroke, as previously described (Pollak et al., 2012). The test was performed at baseline, twice a week for the first 4 weeks post-surgery, and once a week between 5 and 7 weeks post-surgery. A plexigass ladder measuring 30 inches across and rungs 0.25 inches apart was supported on side platforms and filmed from underneath. Mice underwent four training sessions (two transverses across the ladder per session) on the ladder before testing commenced. For each testing session, mice transversed the ladder twice. Each video was scored for correct and missed steps. Data is presented as percent correct foot placement versus total foot placement.

Statistical analysis

Multiplex immunoassays were performed with blinding to experimental condition. However, blinding was not possible for immunostaining experiments because of the infarcts being visible in stroked and MI mice. Statistical analyses were performed with Prism 6.0 software

(GraphPad). Data are expressed as mean ± standard error of the mean (SEM). For multiplex immunoassay experiments, differences between the two experimental groups were analyzed by a Student's t-test with correction for multiple comparisons. Differences between three or more experimental groups were analyzed by one-way ANOVA followed by *post-hoc* Tukey's testing. Significance was set at *$p<0.05$, **$p<0.01$, ***$p<0.001$, and ****$p<0.0001$.

Results

We have previously demonstrated that liquefactive necrosis is imperfectly segregated from uninfarcted brain tissue by glial scars, and that it intensifies post-stroke injury in the weeks after stroke (Zbesko et al., 2018). However, the reason why the brain undergoes liquefactive necrosis in response to ischemia, and why the infarct remains in a liquefactive state for weeks following stroke is unknown. Therefore, in order to improve our understanding of why the brain responds to ischemia by liquefactive necrosis rather than coagulative necrosis, which is the more typical response to ischemia that occurs in other tissues (Robbins et al., 2010), we first compared the kinetics and characteristics of the inflammatory response to ischemia in both the brain and the heart. Mice underwent experimentally induced stroke or myocardial infarction and were sacrificed 24 hours, 1 week, 4 weeks, and 8 weeks later (**Figure 1A**). Tissue was processed for multiplex immunoassay and immunohistochemistry.

Each model of ischemia produced a large infarct of comparable size, and as expected, there was extensive tissue remodeling in both organs in the weeks following ischemia (**Figure 1B**). However, although the acute cytokine responses were broadly similar within the infarcted tissue in both the brain and the heart, the chronic inflammatory responses differed significantly. In both tissues, the initial cytokine response subsided within 4 weeks. However, a second wave of pro-inflammatory cytokine expression appeared between weeks 4 and 8 in the brain. This was

evidenced by a significant increase in the levels of multiple inflammatory cytokines including IP-10, KC, MCP-1, MIP-1α, MIP-1β, MIP-2, RANTES, IL-9, IL-4, and IL-12(p70) within the infarct at 8 weeks post stroke when compared to naïve brain tissue (**Figure 1C**).

Furthermore, although there was substantial immune cell infiltration in both the brain and heart at 1 week following ischemia, by 4 weeks following ischemia, there was a clear discrepancy in the amount of immune cell infiltration and fibrosis present within each type of infarct (**Figure 1D**). In comparison to the brain, the heart infarcts contained markedly more collagen and substantially fewer T-lymphocytes, B-lymphocytes, and CD68+ macrophages at 4 weeks following ischemia. This difference was also evident at 8 weeks following ischemia (**Figure 1E**). There was also no apparent reduction in immune cell infiltration or any apparent increase in collagen deposition in the brain infarcts between 4 weeks and 8 weeks following ischemia. These data indicate that liquefaction of the brain following stroke correlates with a second wave of cytokine expression, scant collagen deposition, and more extensive chronic immune cell infiltration than occurs in the heart following a myocardial infarction.

To understand why the second wave of cytokine expression develops in the infarct in the weeks following stroke, and why the chronic immune cell infiltrate is more substantial and sustained, we looked closely at the configuration of cytokines that were significantly elevated at the 8-week time point. Our findings revealed a molecular fingerprint reminiscent of the cytokine profile present in atheroma. Specifically, IP-10, KC, MCP-1, MIP-1α, MIP-1β, MIP-2, RANTES, IL-9, IL-4, and IL-12(p70) have all been found in atherosclerotic plaques (Braunersreuther et al., 2007; Ramji and Davies, 2015). Significantly, blocking IP-10 and MCP-1 results in atherosclerosis regression in mice (Braunersreuther et al., 2007). Our previous data demonstrate that the human brain at the stage of liquefactive necrosis also contains increased levels of IP-10, MCP-

1, MIP-1α, MIP-1β, and IL12(p70) (Nguyen et al., 2016). Therefore, liquefaction of the brain following stroke shares several cytokine characteristics with atherosclerosis.

In light of this overlap in the cytokine profile between liquefactive necrosis of the brain following stroke and atherosclerosis, we hypothesized that the sustained state of liquefactive necrosis in response to stroke may be due to cholesterol crystal formation within macrophages that engulf cholesterol rich myelin debris. To test this hypothesis, we evaluated the macroscopic (**Figure 2A**) and microscopic (**Figure 2B-C**) features of liquefactive necrosis and looked for the presence of cholesterol crystals (**Figure 2D-I**). As expected, scanning electron microscopy (EM) revealed that liquefactive necrosis is predominantly comprised of a sea of foamy macrophages morphologically similar to the foam cells found in atherosclerotic lesions (**Figure 2B-C**). Transmission EM revealed that each macrophage contains an abundance of lipid droplets (**Figure 2D**). Importantly, transmission EM also provided evidence that many of these macrophages contain cholesterol crystals (**Figure 2E**).

Cholesterol crystals are birefringent and change the polarization of transmitted light (Kashiwagi et al., 2014). Therefore, to validate that macrophages in areas of liquefactive necrosis contain cholesterol crystals, we imaged the 24 hour, 1 week, 4 week, and 8 week-old stroke infarcts using polarized light microscopy. This revealed that birefringent crystals appear within stroke infarcts between weeks 1 and 4 following stroke, and are even more abundant at 8 weeks following stroke (**Figure 2F-G**). This timeline of appearance of crystals correlates with the second wave of cytokine expression within the infarct and the failure of the immune cell infiltrate to resolve between 4 weeks and 8 weeks following stroke, as occurs in the heart.

Although transmission EM and polarized light microscopy are gold standard techniques for the identification of cholesterol crystals (Kashiwagi et al., 2014), we also biochemically identified

these crystals as comprised of cholesterol based on their equilibrium density sedimentation. Cholesterol crystals are known to have a density of 1.04 g/ml (Tangirala et al., 1994). Crystals isolated from cells extracted from areas of liquefactive necrosis 7 weeks following stroke had heterogeneous needle-like and plate-like morphologies, which matches the physical description of cholesterol crystals (Tangirala et al., 1994) (**Figure 2H**), and they sedimented in fractions ranging from 1.030-1.059g/ml, in agreement with the expected density of cholesterol crystals (**Figure 2I**). These experiments provide evidence that chronic liquefactive necrosis of the brain in response to stroke is associated with the accumulation of cholesterol crystals.

To determine if liquefaction of the brain following stroke shares other characteristics with atherosclerosis we measured the levels of OPN, IL-18, MMP-2, MMP-3, and MMP-8. The rationale for measuring OPN is that it is one of the most abundant proteins present within atheroma and is expressed at high levels in other crystallopathies (Khan et al., 2002). The rationale for measuring IL-18 is that cholesterol crystals activate the NLRP3 inflammasome in atheroma, and IL-18 is a hallmark of inflammasome activation (Duewell et al., 2010; Baldrighi et al., 2017; Hoseini et al., 2017; Karasawa and Takahashi, 2017). The rationale for evaluating levels of MMP-2, MMP-3, and MMP-8 is that cholesterol crystals induce MMP expression in macrophages and MMPs are abundant in atheroma (Beaudeux et al., 2004; Watanabe and Ikeda, 2004; Lenglet et al., 2013; Corr et al., 2016). Multiplex immunoassay analyses revealed that OPN is present at markedly high levels in areas of liquefactive necrosis (**Figure 3A**), that IL-18 is also present (**Figure 3B**), and that there are also strikingly high levels of MMP-2, MMP-3, and MMP-8 (**Figure 3C-E**).

We next tested if the formation of cholesterol crystals and the high expression of MMPs in areas of liquefactive necrosis is specific to C57BL/6 mice or specific to DH stroke. BALB/c mice underwent DMCAO without hypoxia and were sacrificed 7 weeks later. These mice also

developed birefringent crystals in the infarct in the weeks after stroke (**Figure 4A-B**), and had abundant expression of MMP-2, MMP-3, and MMP-8 (**Figure 4C**) in the area of liquefaction 7 weeks following stroke. The formation of cholesterol crystals in chronic stroke infarcts is not mouse strain or stroke model dependent.

Even though liquefactive necrosis is imperfectly contained by glial scarring and intensifies post-stroke injury (Zbesko et al., 2018), it is currently unknown how long it takes for liquefactive necrosis to resolve in the brain after stroke. Therefore, C57BL/6 mice underwent DH stroke and were sacrificed 24 weeks later. Immunostaining revealed a substantial reduction in CD3+ T-lymphocyte, B220+ B-lymphocyte, and CD68+ macrophage infiltration at 24 weeks following stroke, and trichrome staining demonstrated an increase in collagen scarring (**Figure 5A**). Multiplex immunoassay determined that cytokine levels in the infarct at 24 weeks were substantially and significantly lower compared to the corresponding areas of cortex from mice sacrificed 8 weeks following stroke (**Figure 5B**). Levels of MMP-2, MMP-3, and MMP-8 were also substantially reduced and had returned to baseline levels (**Figure 5C**). Based on these data, liquefactive necrosis is resolved by 24 weeks following stroke in young adult C57BL/6 mice.

We then tested if targeting intermediaries in the pathophysiology of atherosclerosis using genetically modified mice could mitigate the production of cytokines and proteases within chronic stroke infarcts and improve stroke outcome. The intermediaries targeted were NLRP3 using NLRP3 deficient mice, CD36 using CD36 deficient mice, and OPN using OPN deficient mice. The rationale for NLRP3 was that we hypothesized that the genetic ablation of NLRP3 would prevent the activation of the NLRP3 inflammasome by cholesterol crystals. CD36 is a scavenger receptor involved in both cholesterol uptake by macrophages and inflammasome activation in atherosclerosis (Stewart et al., 2010; Kagan and Horng, 2013; Park, 2014), and

OPN regulates macrophage chemotaxis (Lund et al., 2013), as well as the production of MMPs by macrophages (Mi et al., 2007) (**Figure 6A**).

NLRP3$^{-/-}$, CD36$^{-/-}$, and OPN$^{-/-}$ mice underwent DH stroke and were sacrificed 7 weeks later. The levels of cytokines and MMPs in the area of liquefaction were then analyzed by multiplex immunoassay and compared to wt mice. Levels of IL-1α and IL-1β were significantly reduced in the NLRP3$^{-/-}$ mice (**Figure 6B**), however other cytokine levels and MMP levels were unchanged (**Figure 6C**). There were no changes in cytokine or MMP levels in the CD36$^{-/-}$ mice except for a reduction in TNF- α (**Figure 6B-C**). The biggest change in the levels of cytokines and MMP levels was evident in the OPN$^{-/-}$ mice. G-CSF, IL-12(p70), IP-10, MCP-1, MIP-1α, MIP-1β, RANTES, TNF- α, MMP-2, and MMP-8 were all significantly and substantially reduced (**Figure 6B-C**).

Based on the considerable reduction in cytokine and protease expression present in the area of liquefaction in the OPN$^{-/-}$ mice we next determined if this correlated with an improvement in recovery and a reduction in secondary neurodegeneration. We have previously shown that infarct size following stroke is equivalent in OPN-/- and wt mice (Doyle et al., 2008). However, compared to wt mice, OPN$^{-/-}$ mice recovered motor function significantly faster following DH stroke (**Figure 7A**) than wt mice, and exhibited a greater preservation of neurons in the peri-infarct location as evinced by increased neuronal marker, NeuN, immunoreactivity (**Figure 7B-D**).

Discussion (1500 Words)

Using mouse models of myocardial infarction and ischemic stroke, we tested whether the brain takes longer to heal from ischemic injury than the heart. Using these models, we demonstrated that the inflammatory response to ischemic injury in the brain takes longer to resolve than the inflammatory response to a similar injury in the heart. Further, in the brain we observed a biphasic cytokine response to ischemia, with the second phase initiated between weeks 4 and 8 after ischemic injury. In common with the pathogenesis of atheroma, the second phase included a predominance of foamy macrophages and the presence of T-lymphocytes. Importantly the second phase of inflammation coincided with the accumulation of intracellular and extracellular cholesterol crystals within the infarct.

Cholesterol crystals can activate the NLRP3 inflammasome. Congruently, we found evidence of NLRP3 inflammasome activity within ischemic stroke infarcts during the chronic stage of liquefactive necrosis, as supported by a significant elevation of IL-18 at 8 weeks following stroke. In contrast, elevated IL-18 was not detected in the heart following myocardial infarction. We also examined MMP expression given the known association of MMPs with atherosclerotic plaque, and their potential participation in liquefaction of the necrotic tissue. There was chronic and abundant expression of MMP-2, MMP-3, and MMP-8 in the area of liquefactive necrosis following stroke compared to the equivalent area of infarction in the heart. Indeed, expression of MMP-2 was 100-fold higher (4,273 pg/mg), expression of MMP-3 was almost 3000-fold higher (15,059 pg/mg), and expression of MMP-8 was 500-fold higher (12,923 pg/mg) at 8 weeks post stroke in the area of liquefactive necrosis compared to naïve brain tissue.

MMP-2 is a gelatinase, MMP-3 is a stromelysin, and MMP-8 is a collagenase (Amin et al., 2016), and such proteases digest proteins to amino acids. The chronically high expression of MMPs is a probable mechanism through which the solid tissue of the brain liquifies and remains

liquefactive for months following stroke. Further, this may be an explanation for the much later collagen deposition that occurs in the brain compared to the heart.

MMPs can degrade myelin and so the initial high production of MMP-2, MMP-3, and MMP-8 at 24 hours following stroke likely occurs as a microglia/macrophage response to damaged myelin (Chandler et al., 1995; D'Souza et al., 2002). However, the overproduction of MMPs in the central nervous system is neurotoxic due to their capacity to disrupt tight junctions and degrade intact myelin on healthy neurons. Furthermore, MMP-2 converts stromal cell derived factor 1 (SDF-1), which is produced by reactive astrocytes, into a highly neurotoxic fragment (Zhang et al., 2003; Fujimoto et al., 2008; Mroczko et al., 2013). Other degradative enzymes are also likely to be substantially and chronically elevated in areas of liquefactive necrosis following stroke. The full characterization of this repertoire is likely to reveal additional targets for reducing secondary neurodegeneration.

Macrophages produce MMPs not only in response to damaged myelin, but also in response to cholesterol crystals (Corr et al., 2016). This finding is surprising because MMPs target proteins rather than lipids. Nevertheless, Corr and colleagues have shown that the treatment of primary macrophages with cholesterol crystals leads to crystal ingestion and activation of Syk and PI3K within minutes, followed by an over 500-fold increase in MMP-1 production (Corr et al., 2016). This may be because extracellular cholesterol crystals are able to activate the foreign body response. The foreign body response leads to the formation of multinucleated giant cells that generate large amounts of MMPs and other proteolytic enzymes (Anderson et al., 2008; McNally et al., 2008). Giant cells can engulf and digest large particles, or if the particles are too large for engulfment, they mediate bulk digestion via the extracellular release of degradative enzymes (Sheikh et al., 2015). In the 1970s, Bayliss performed a time course study in which he demonstrated that giant cells can convert cholesterol crystals injected

subcutaneously into Wistar rats into droplets of esterified cholesterol over a period of 3 months (Bayliss, 1976). This provides a link between the presence of myelin debris and cholesterol crystals in chronic stroke infarcts, the sustained production of MMPs, and ultimately the clearance of cholesterol crystals and the resolution of liquefactive necrosis.

In this study, we discovered that liquefactive necrosis is resolved by 24 weeks in young adult C57BL/6 mice, however, in light of Cantuti-Castelvetri et al's recent finding that phagocytes from aged animals are less able to process myelin debris than young animals, aged mice may take considerably longer (Cantuti-Castelvetri et al., 2018). How long it takes for liquefactive necrosis to resolve in humans is still unknown and should be investigated as a high priority. It is probable that it is influenced by age, comorbidities, genetics, infarct size, and stroke location, and it is also likely that it is causing different amounts of secondary neurodegeneration in different patients.

Further emphasizing the need for such studies, although it has yet to be fully characterized the extent to which humans form cholesterol crystals in the brain following stroke, in 1987 Miklossy and Van der Loos reported that crystals of cholesterol esters are present for at least 20 months in the human brain after stroke, both within the area of infarction, as well as the tracts originating in, and passing through the region of infarction (Miklossy and Van der Loos, 1987; Miklossy et al., 1991).

The cytokine profile in the area of liquefactive necrosis resembles the cytokine profile present in atheroma (Braunersreuther et al., 2007). For example, there is the chronic presence of MCP-1, IP-10, and RANTES, known participants in atheroma. Our previous data demonstrate that the human brain at the stage of liquefactive necrosis also contains many of the cytokines found in atheroma including MCP-1, IP-10, MIP-1α, and MIP-1β, (Nguyen et al., 2016). The presence of

these cytokines not only demonstrate overlap between the molecular profile of atherosclerosis and liquefactive necrosis, they also provide additional targets for intervention. For instance, blocking MCP-1, IP-10, and RANTES results in atherosclerosis regression in mice (Braunersreuther et al., 2007). With regard to the relative abundance of the cytokines present in the area of liquefactive necrosis, of the cytokines we analyzed, the most abundant cytokine was OPN. OPN is also one of the most abundant cytokines expressed in atheroma (Scatena et al., 2007).

There is a direct link between OPN and MMP expression. Extracellular MMP inducer (EMMPRIN) is an upstream inducer of several MMPs and is a master regulator of MMP production (Agrawal and Yong, 2011). The COOH-terminus of OPN, which is released upon thrombin cleavage and contains a cryptic SLAYGLR motif, is an EMMPRIN agonist. Specifically, the thrombin cleaved COOH-terminal fragment of OPN forms a complex with cyclophilin C, which upon engagement of EMMPRIN has been shown in murine mammary epithelial tumor cell lines to lead to phosphorylation of Akt and MMP-2 activation and secretion (Mi et al., 2007). Cyclophilin C and cyclophilin-C-associated protein (CyCap) are expressed by macrophages in response to tissue damage (Kong et al., 2007), and in the brain, cyclophilin C complexes with CyCap to activate microglia via the calcineurin/NFAT pathway (Yamaguchi et al., 2011). This may explain why MMP-2 and MMP-8 levels were substantially reduced in the infarct in the OPN deficient mice.

Further supporting a critical role of OPN in the mechanism of liquefactive necrosis, OPN is important in promoting the retention of macrophages at sites of chronic inflammation (Scatena et al., 2007), and is known to regulate chronic inflammatory responses to foreign bodies. This is evidenced by the fact that renal epithelial cells increase the production of osteopontin in response to exposure to calcium oxalate crystals (Khan et al., 2002), there are deficits in

macrophage accumulation in $OPN^{-/-}$ mice in models of biomaterial implantation (Scatena et al., 2007), and Oh and colleagues recently demonstrated that the thrombin cleaved COOH-terminal fragment of OPN plays a role in multinucleated giant cell formation (Oh et al., 2014).

With regard to therapeutic intervention, G-CSF, IL-12, IP-10, MCP-1, MIP-1α, MIP-1β, RANTES, TNF-α, MMP-2, and MMP-8 were substantially reduced in $OPN^{-/-}$ mice 7 weeks following stroke, and these mice exhibited less secondary neurodegeneration in the peri-infarct location. Although the administration of OPN acutely is neuroprotective (Meller et al., 2005; Doyle et al., 2008), these data suggest that reducing OPN activity in the chronic inflammatory process may be a promising target for therapeutic intervention in recovering stroke patients. In further support of this it has already been shown that OPN deficiency attenuates MMP activity and plaque accumulation in mouse models of atherosclerosis (Bruemmer et al., 2003; Matsui et al., 2003).

Surprisingly, genetically ablating the NLRP3 inflammasome, which is activated by intracellular cholesterol crystals, had little impact on cytokine production or the MMP response to stroke. Although IL1 levels were reduced in the area of liquefaction as expected, no other protein measured in this study was altered. This unexpected result suggests that the NLRP3 inflammasome is less integral to the pathophysiology of liquefactive necrosis than OPN. A potential explanation for this result is that NLRP3 is not required for the full development of the foreign body response (Malik et al., 2011).

An additional explanation is that there may be another consequence of myelin debris clearance other than the formation of cholesterol crystals that prevents the inflammatory response to stroke from resolving as efficiently as the inflammatory response to myocardial infarction. A

possible example is the formation of oxysterols. Oxysterols are a product of cholesterol processing in foam cells, and they are another important driver of inflammation in atherosclerotic lesions (Gargiulo et al., 2011; Poli et al., 2013). More research is needed to determine the relative contributions of cholesterol crystals, oxysterols, and other myelin debris metabolites to the pathogenicity of chronic stroke infarcts.

CD36 is a key regulator of lipid droplet formation in atherogenesis due to its ability to bind to lipoproteins, oxidized phospholipids, fatty acids, and oxidized low density lipoprotein. However, in this study the genetic ablation of CD36 had little impact on chronic cytokine production and MMP expression after stroke. This lack of an effect may be due to redundancy in scavenger receptor expression on the surface of microglia and macrophages.

In conclusion, myelin has evolved to form a stable and long-lived insulating sheath that is difficult to degrade (Schmitt et al., 2015). Consequently, following a sizable CNS insult such as a stroke, the production of myelin debris and the release of the associated cholesterol appears to overwhelm the cholesterol degradation capacities of phagocytosing microglia and macrophages. Thus, treatments that target cholesterol overloading within macrophages and the sustained production of degradative enzymes may help to prevent the damaging effects of liquefactive necrosis following stroke.

Acknowledgments: This work was funded by NIH K99NR013593 (KPD), NIH R01NS096091 (KPD), and start-up funding provided by the University of Arizona, Tucson, AZ.

Ethical approval

All applicable international, national, and/or institutional guidelines for the care and use of

animals were followed. As such, all experiments were conducted in accordance with protocols approved by the Animal Care and Use Committee of the University of Arizona and were performed based on the NIH Guide for the Care and Use of Laboratory Animals.

Conflict of interest: The authors declare that they have no conflict of interest.

Figures

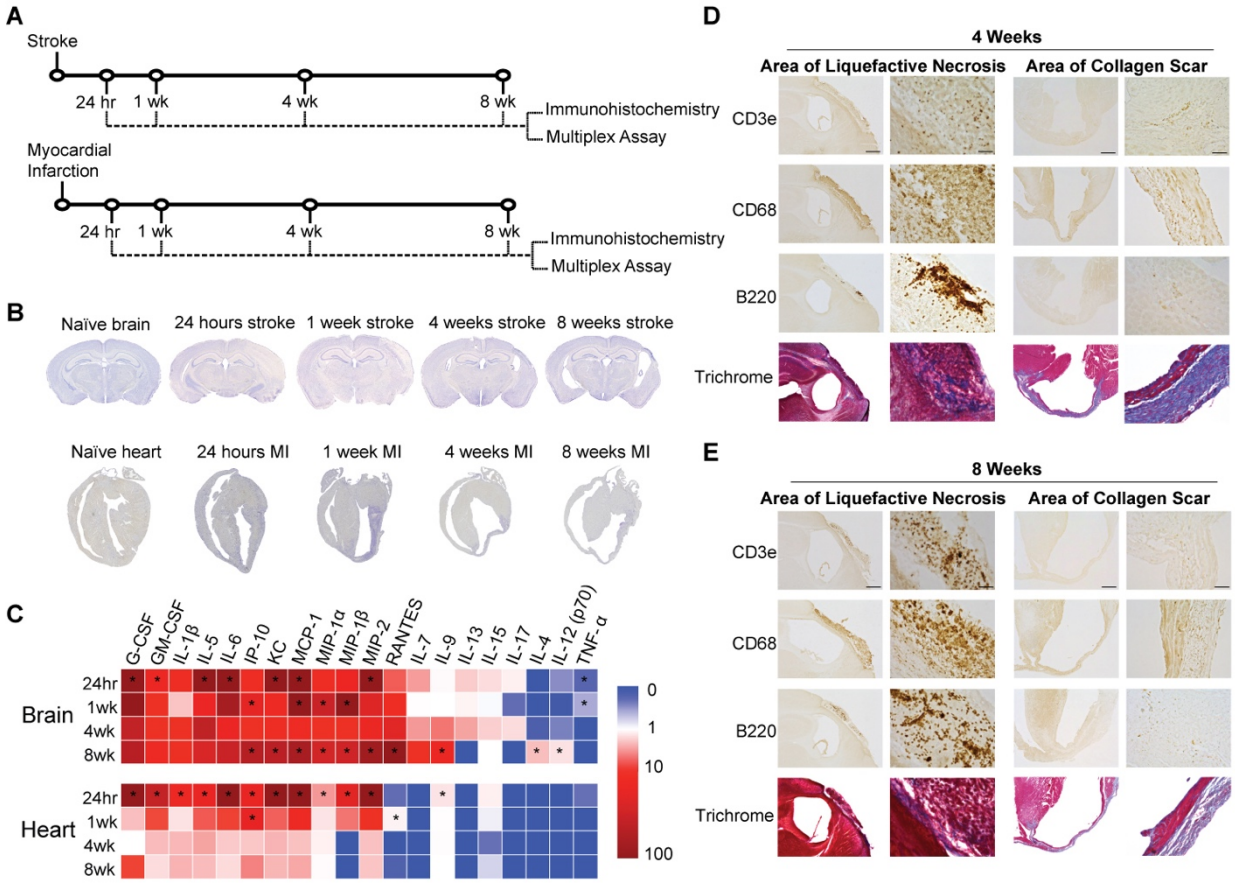

Fig. 1. The inflammatory response to ischemic injury is slower to resolve in the brain compared to the heart. (**A**) Experimental design. Mice were either given a stroke or myocardial infarction and were euthanized 24 hours, 1 week, 4 weeks, or 8 weeks following surgery. Infarcted tissue was dissected and processed for analysis by either immunohistochemistry or multiplex immunoassay. (**B**) Nissl staining demonstrates tissue morphology following the respective models of ischemia in the brain and heart. (**C**) Heat map of inflammatory marker expression detected by multiplex immunoassay in the brain and heart at 24 hours, 1 week, 4 weeks, and 8 weeks following ischemia. Values are expressed as fold change relative to naïve heart and brain controls. *$p<0.05$ compared to naïve tissue controls. (**D**) Comparison of immune

cells present in the infarct in the brain and heart at 4 weeks following ischemic injury. There is more extensive infiltration of T-lymphocytes (CD3e; top row), macrophages (CD68; second row), and B-lymphocytes (B220; third row) in the brain compared to the heart. Conversely, there is much more collagen deposition (blue staining; bottom row) in the heart, compared to the brain. (**E**) Comparison of immune cells present in the infarct in the brain and heart at 8 weeks following ischemic injury. Scale bar, 500 μm for low (4x) magnification images, and 50 μm for high (20x) magnification images. n=5-7 mice per time point and assay.

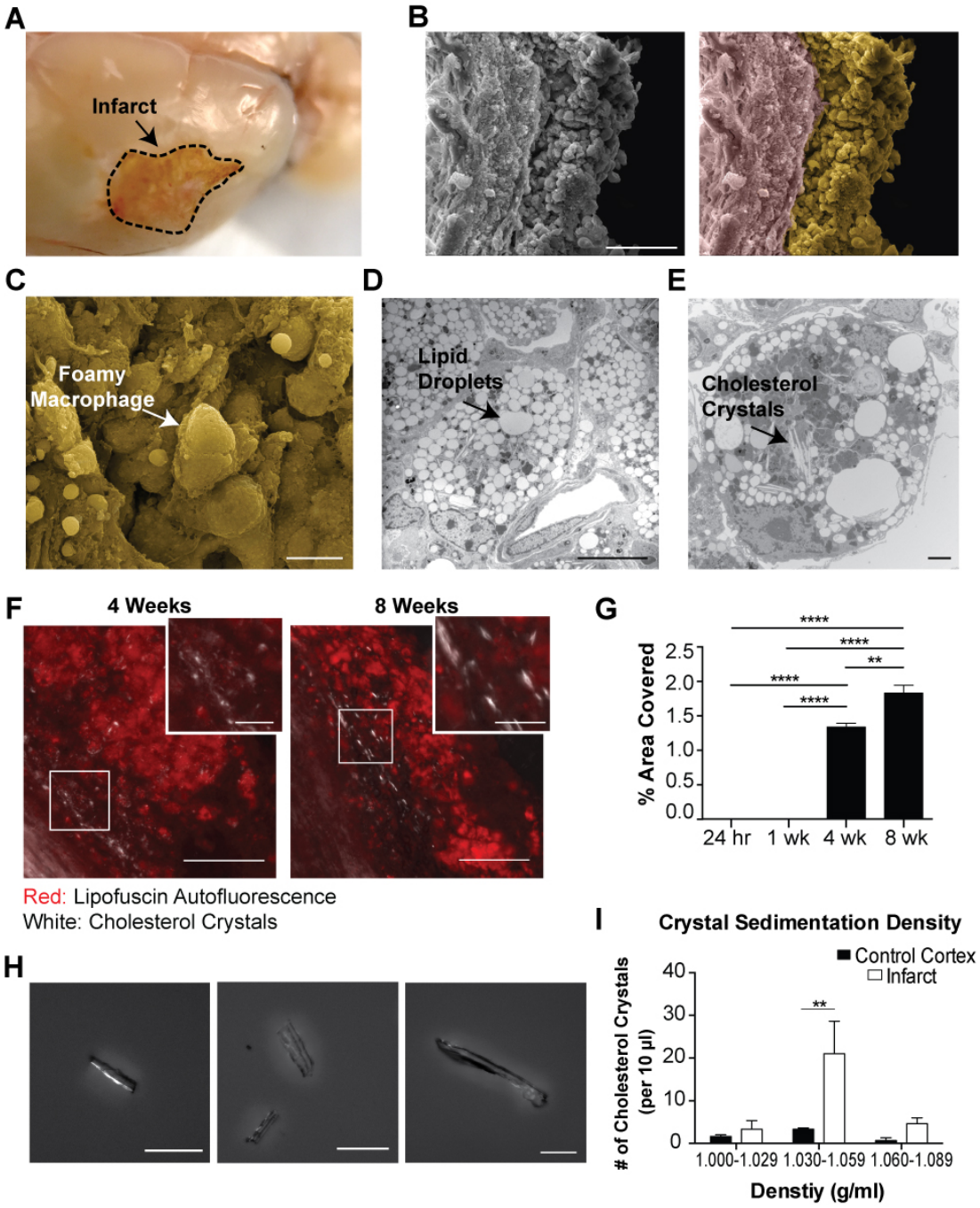

Fig. 2. Foamy macrophages within areas of liquefactive necrosis contain cholesterol crystals. (**A**) Gross pathology of a lesion (delineated) 7 weeks following stroke. The infarcted area is in a liquefactive state. (**B**) Original (left image) scanning EM image of a 7-week infarct with a dense population of cells (pseudocolored yellow; right image) and glial scar

(pseudocolored purple; right image). Scale bar, 100 μm. The infarct is filled with foamy macrophages (arrow), as seen magnified in (**C**). Scale bar, 50 μm. (**D**) Transmission EM of a macrophage in the infarct at 7 weeks following stroke. There is an accumulation of lipid droplets (arrow), providing the macrophage with its characteristic foamy appearance. Scale bar, 10 μm. (**E**) Transmission EM of a foamy macrophage in the infarct at 7 weeks following stroke with putative cholesterol crystal clefts in the cytoplasm (arrow). Scale bar, 2 μm. (**F**) Confirmation of the presence of cholesterol crystals (white) in the infarct by overlaying images taken with polarized and fluorescence microscopy. Lipofuscin autofluorescence (red) demarcates the area of infarction. Scale bar, 100 μm. Inset scale bars, 25 μm. (**G**) Quantification of cholesterol crystals in the lesion at 24 hours, 1 week, 4 weeks, and 8 weeks following stroke. Data represents mean ± SEM from n=4-5 mice per experimental group. **$p<0.01$ and **** $p<0.0001$. (**H**) Cholesterol crystals, purified from 7-week infarcted brains using sucrose density gradient centrifugation, and visualized under polarized microscopy. Cholesterol crystals were identified by the presence of light refraction. Scale bar, 50 μm. (**I**) The number of cholesterol crystals present in fractionated densities from chronic stroke infarcts or the equivalent area on the contralateral hemisphere (control cortex). Data represent mean ± SEM from n=3 sucrose density gradient centrifugation runs with n=5-10 mice per experiment. **$p<0.01$.

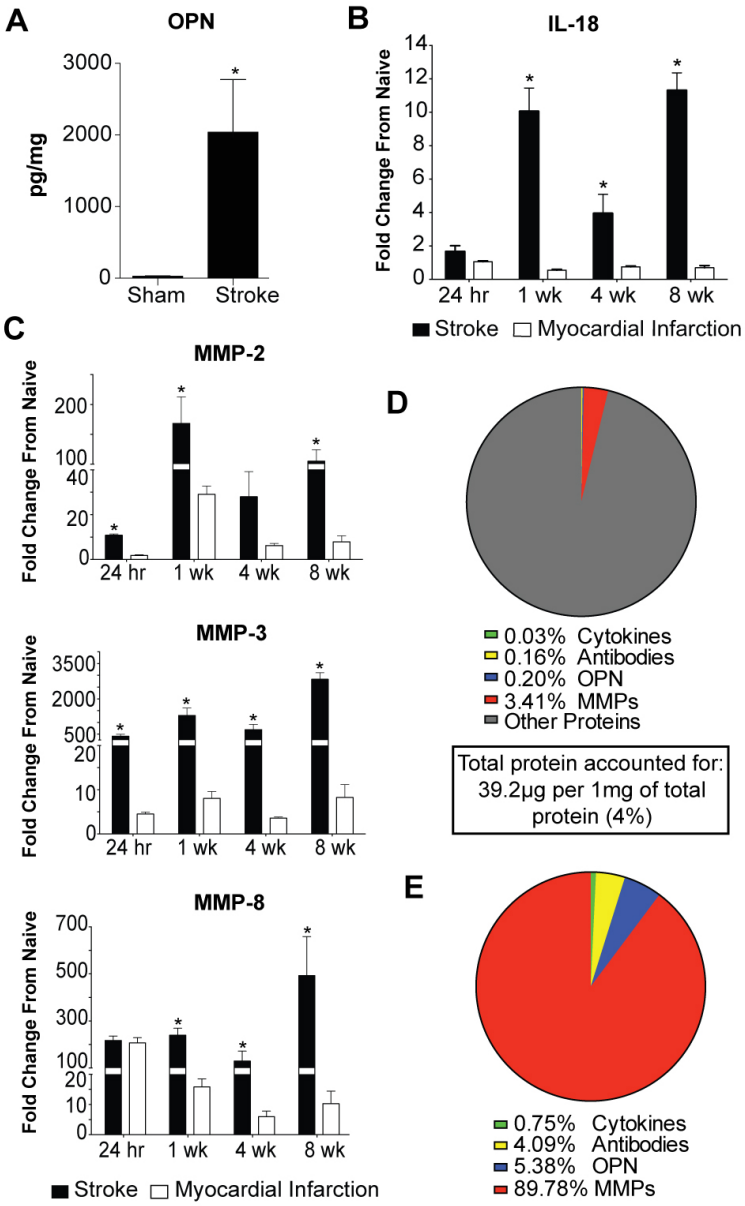

Fig. 3. Liquefaction of the brain following stroke shares multiple characteristics with atherosclerosis. (**A**) There is a significant elevation of OPN in the area of liquefactive necrosis at 7 weeks following stroke compared to the equivalent area in the cortex from sham mice. Data represent mean ± SEM from n=6 mice per experimental group. (**B**) There is significant elevation of IL-18 in the brain infarct at 1 week, 4 weeks, and 8 weeks following ischemic injury compared to the heart infarct. A biphasic elevation of IL-18 is seen in brain infarcts which peaks at 1 week

and 8 weeks following stroke. (**C**) MMP-2 levels are significantly elevated within the brain infarct at 24 hours, 1 week, and 8 weeks following ischemic injury compared to the heart infarct. MMP-3 levels are significantly elevated within the brain infarct at 24 hours, 1 week, 4 weeks, and 8 weeks following ischemic injury compared to the heart infarct. MMP-8 levels are significantly elevated within the brain infarct at 1 week, 4 weeks, and 8 weeks following ischemic injury compared to the heart infarct. *$p<0.05$. (**D**) Pie chart illustrating the relative percentage of total identified protein, cytokines, antibodies, OPN, and MMPs in 1mg of liquefactive necrosis. Cytokine, OPN, and MMP concentrations are from the data generated in this study. Antibody concentrations were taken from our previously published work (Doyle et al., 2015) (**E**) Pie chart illustrating the dominance of MMP expression, by percentage, amongst the identified inflammatory molecules we have measured in areas of liquefactive necrosis.

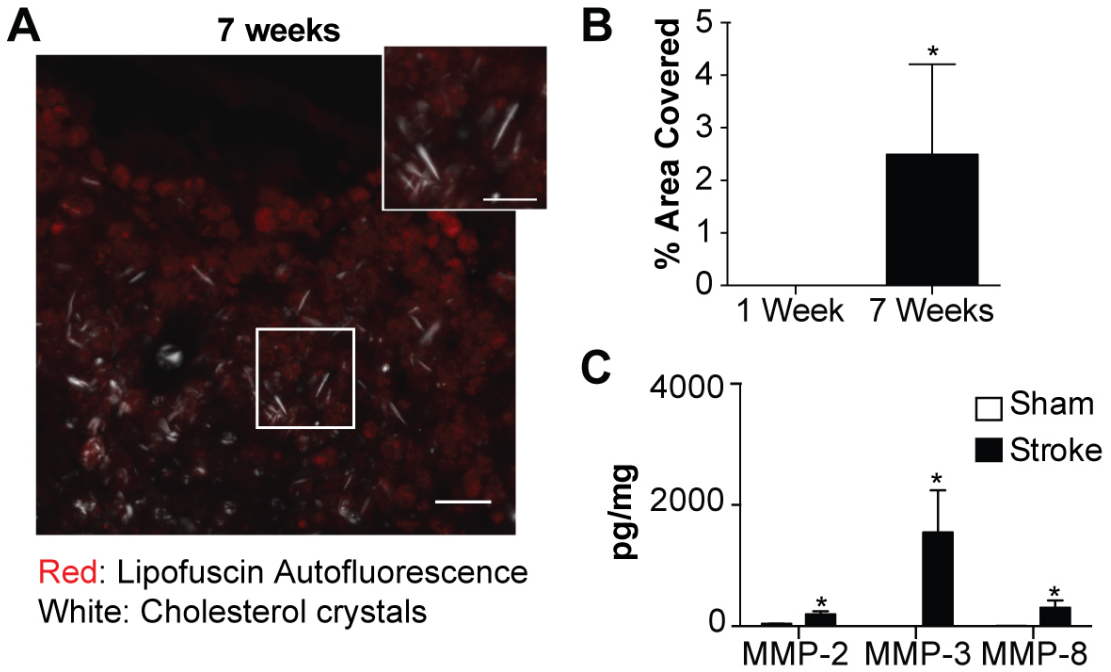

Fig. 4. Cholesterol crystals and MMPs also accumulate in the area of liquefactive necrosis following stroke in BALB/c mice. (**A**) Cholesterol crystals present in the infarct (delineated) at 7 weeks following stroke, visualized using polarized microscopy overlayed with fluorescence microscopy. Lipofuscin autofluorescence (red) denotes the lesion. Scale bar, 50 μm. Inset scale bar, 25 μm. (**B**) Cholesterol crystals accumulate in the infarct between 1 week and 7 weeks following stroke. (C) Levels of MMP-2, MMP-3, and MMP-8 are significantly increased in the infarct of stroked BALB/c mice compared to an equivalent area of the cortex in sham mice. *$p<0.05$.

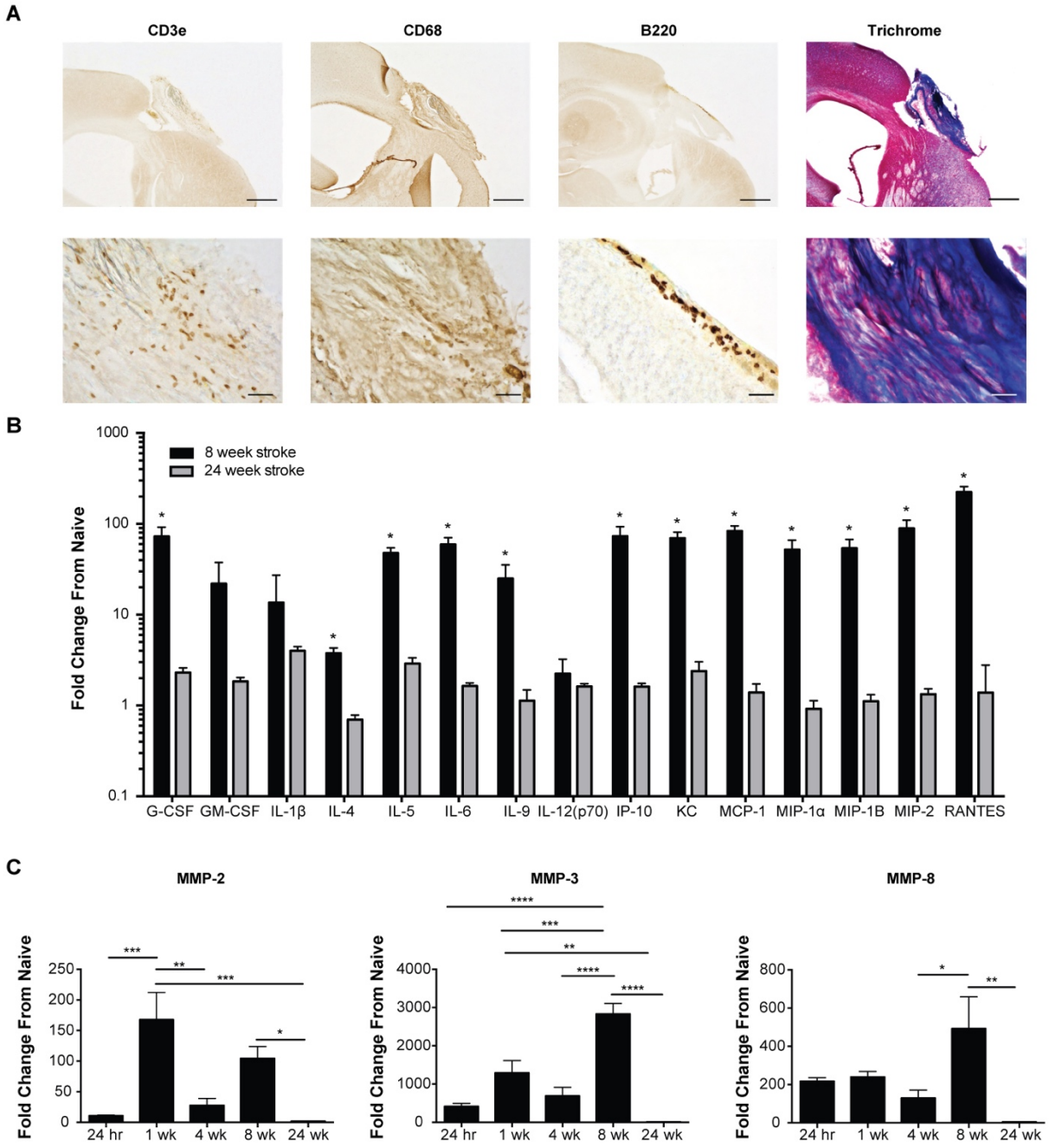

Fig. 5. Liquefactive necrosis subsides and a collagen scar is formed by 24 weeks following stroke in C57BL/6 mice. (**A**) Top panels show representative images of immune cell infiltration and collagen deposition in brain infarcts at 24 weeks post-stroke. Scale bar, 500 μm. Bottom panels show higher magnification images. Scale bar, 50 μm. There is a decrease in the

number of T-lymphocytes (CD3e; left panel), macrophages (CD68; first middle panel), and B-lymphocytes (B220; second middle panel) in the infarct 24 weeks following stroke compared to 8 weeks. There is also a marked increase in collagen (Trichrome; blue) staining at 24 weeks following stroke compared to 8 weeks. (**B**) Multiplex immunoassays demonstrate a concomitant decrease in cytokines/chemokines within the infarct at 24 weeks following stroke compared to 8 weeks following stroke. (**C**) Multiplex immunoassays indicate that MMP levels within the infarct have also returned to baseline levels at 24 weeks following stroke. Data represents mean ± SEM from n=5-6 mice per experimental group. Fold change compared to naïve tissue controls. *$p<0.05$, **$p<0.01$, ***$p<0.001$, and ****$p<0.0001$.

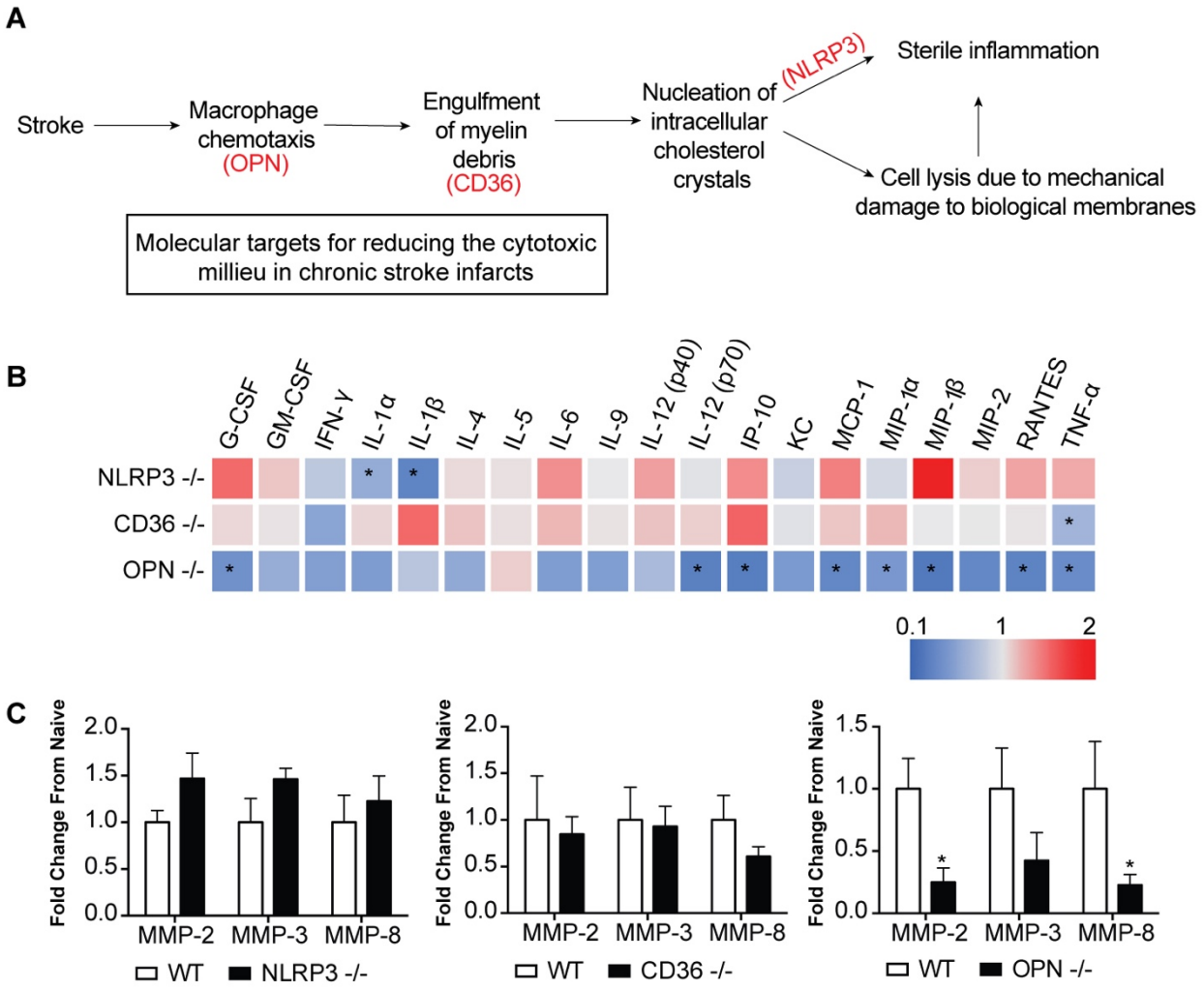

Fig. 6. Molecular targets for reducing the cytotoxic milieu in chronic stroke infarcts. (**A**) Rationale for targeting OPN, CD36, and NLRP3 as a means of reducing the inflammatory response in areas of liquefactive necrosis following stroke. (**B**) Heat map of the levels of inflammatory markers in infarcted brain obtained by multiplex immunoassays demonstrates that the chronic inflammatory response was attenuated the most in OPN$^{-/-}$ mice. NLRP3$^{-/-}$ mice showed a significant reduction in the chronic levels of IL-1α and IL-1β. CD36$^{-/-}$ mice only showed a significant reduction in chronic levels of TNF-α. Data represents mean fold change compared to wt mice. n=6 mice per experimental group. (**C**) Multiplex immunoassays of MMPs

show no significant changes in MMP levels in the chronic infarcts of NLRP3$^{-/-}$ (left graph) and CD36$^{-/-}$ (middle graph) mice compared to wt mice. MMP levels are significantly and substantially lower in the chronic infarct of OPN$^{-/-}$ mice (right graph) compared to wt mice. Data represents mean ± SEM from n=6 mice per experimental group. *$p<0.05$.

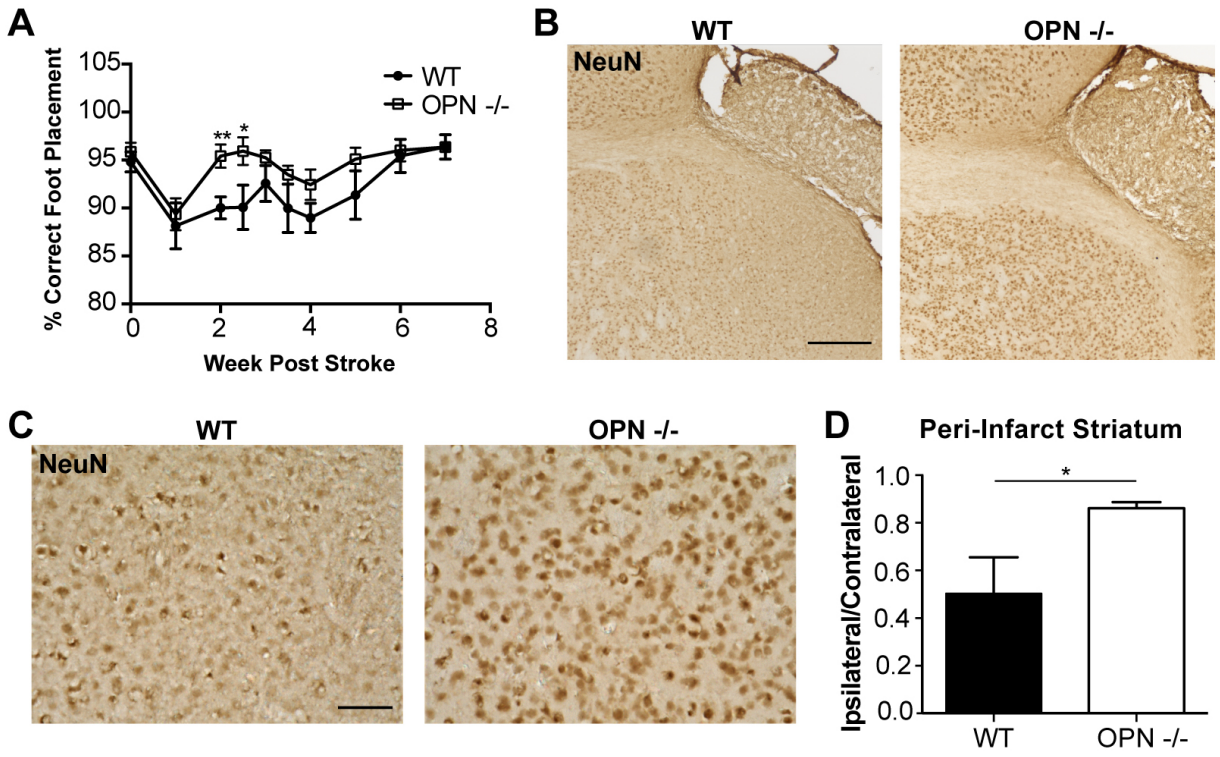

Fig. 7: Genetic ablation of OPN improves recovery and reduces secondary neurodegeneration following stroke. (**A**) Ladder rung tests were scored twice per week for the first 4 weeks following stroke and weekly thereafter. OPN$^{-/-}$ mice were able to recover faster on the ladder rung test compared to wt mice. mice. *p<0.05 and **p<0.01. (**B**) Representative images showing preservation of neuronal marker NeuN immunoreactivity in the peri-infarct area of OPN$^{-/-}$ mice compared to wt mice at 7 weeks following stroke. Scale bar, 250 μm. (**C**) Higher magnification representative images showing preservation of NeuN immunoreactivity in the peri-infarct area of OPN$^{-/-}$ mice. Scale bar, 50 μm. (**D**) Quantitation of NeuN immunoreactivity in the peri-infarct area shows a significant increase in the OPN$^{-/-}$ mice. n = 5-6 per experimental group. Data represents mean ± SEM. *p<0.05.

References

Abela GS, Aziz K (2005) Cholesterol crystals cause mechanical damage to biological membranes: a proposed mechanism of plaque rupture and erosion leading to arterial thrombosis. Clin Cardiol 28:413-420.

Agrawal SM, Yong VW (2011) The many faces of EMMPRIN - roles in neuroinflammation. Biochimica et biophysica acta 1812:213-219.

Amin M, Pushpakumar S, Muradashvili N, Kundu S, Tyagi SC, Sen U (2016) Regulation and involvement of matrix metalloproteinases in vascular diseases. Frontiers in bioscience 21:89-118.

Anderson JM, Rodriguez A, Chang DT (2008) Foreign body reaction to biomaterials. Semin Immunol 20:86-100.

Baldrighi M, Mallat Z, Li X (2017) NLRP3 inflammasome pathways in atherosclerosis. Atherosclerosis 267:127-138.

Bayliss OB (1976) The giant cell in cholesterol resorption. Br J Exp Pathol 57:610-618.

Beaudeux JL, Giral P, Bruckert E, Foglietti MJ, Chapman MJ (2004) Matrix metalloproteinases, inflammation and atherosclerosis: therapeutic perspectives. Clin Chem Lab Med 42:121-131.

Braunersreuther V, Mach F, Steffens S (2007) The specific role of chemokines in atherosclerosis. Thrombosis and haemostasis 97:714-721.

Bruemmer D, Collins AR, Noh G, Wang W, Territo M, Arias-Magallona S, Fishbein MC, Blaschke F, Kintscher U, Graf K, Law RE, Hsueh WA (2003) Angiotensin II-accelerated atherosclerosis and aneurysm formation is attenuated in osteopontin-deficient mice. J Clin Invest 112:1318-1331.

Cantuti-Castelvetri L, Fitzner D, Bosch-Queralt M, Weil MT, Su M, Sen P, Ruhwedel T, Mitkovski M, Trendelenburg G, Lutjohann D, Mobius W, Simons M (2018) Defective cholesterol clearance limits remyelination in the aged central nervous system. Science.

Chandler S, Coates R, Gearing A, Lury J, Wells G, Bone E (1995) Matrix metalloproteinases degrade myelin basic protein. Neuroscience letters 201:223-226.

Corr EM, Cunningham CC, Dunne A (2016) Cholesterol crystals activate Syk and PI3 kinase in human macrophages and dendritic cells. Atherosclerosis 251:197-205.

D'Souza CA, Mak B, Moscarello MA (2002) The up-regulation of stromelysin-1 (MMP-3) in a spontaneously demyelinating transgenic mouse precedes onset of disease. The Journal of biological chemistry 277:13589-13596.

Doyle KP, Fathali N, Siddiqui MR, Buckwalter MS (2012) Distal hypoxic stroke: A new mouse model of stroke with high throughput, low variability and a quantifiable functional deficit. J Neurosci Methods.

Doyle KP, Yang T, Lessov NS, Ciesielski TM, Stevens SL, Simon RP, King JS, Stenzel-Poore MP (2008) Nasal administration of osteopontin peptide mimetics confers neuroprotection in stroke. J Cereb Blood Flow Metab 28:1235-1248.

Doyle KP, Quach LN, Sole M, Axtell RC, Nguyen TV, Soler-Llavina GJ, Jurado S, Han J, Steinman L, Longo FM, Schneider JA, Malenka RC, Buckwalter MS (2015) B-Lymphocyte-Mediated Delayed Cognitive Impairment following Stroke. J Neurosci 35:2133-2145.

Duewell P, Kono H, Rayner KJ, Sirois CM, Vladimer G, Bauernfeind FG, Abela GS, Franchi L, Nunez G, Schnurr M, Espevik T, Lien E, Fitzgerald KA, Rock KL, Moore KJ, Wright SD, Hornung V, Latz E (2010) NLRP3 inflammasomes are required for atherogenesis and activated by cholesterol crystals. Nature 464:1357-1361.

Fujimoto M, Takagi Y, Aoki T, Hayase M, Marumo T, Gomi M, Nishimura M, Kataoka H, Hashimoto N, Nozaki K (2008) Tissue inhibitor of metalloproteinases protect blood-brain barrier disruption in focal cerebral ischemia. J Cereb Blood Flow Metab 28:1674-1685.

Gargiulo S, Sottero B, Gamba P, Chiarpotto E, Poli G, Leonarduzzi G (2011) Plaque oxysterols induce unbalanced up-regulation of matrix metalloproteinase-9 in macrophagic cells through redox-sensitive signaling pathways: Implications regarding the vulnerability of atherosclerotic lesions. Free Radic Biol Med 51:844-855.

Hoseini Z, Sepahvand F, Rashidi B, Sahebkar A, Masoudifar A, Mirzaei H (2017) NLRP3 inflammasome: Its regulation and involvement in atherosclerosis. J Cell Physiol.

Kagan JC, Horng T (2013) NLRP3 inflammasome activation: CD36 serves double duty. Nat Immunol 14:772-774.

Karasawa T, Takahashi M (2017) Role of NLRP3 Inflammasomes in Atherosclerosis. J Atheroscler Thromb 24:443-451.

Kashiwagi M, Liu L, Chu KK, Sun CH, Tanaka A, Gardecki JA, Tearney GJ (2014) Feasibility of the assessment of cholesterol crystals in human macrophages using micro optical coherence tomography. PLoS One 9:e102669.

Khan SR, Johnson JM, Peck AB, Cornelius JG, Glenton PA (2002) Expression of osteopontin in rat kidneys: induction during ethylene glycol induced calcium oxalate nephrolithiasis. J Urol 168:1173-1181.

Kong W, Li S, Longaker MT, Lorenz HP (2007) Cyclophilin C-associated protein is up-regulated during wound healing. J Cell Physiol 210:153-160.

Lenglet S, Mach F, Montecucco F (2013) Role of matrix metalloproteinase-8 in atherosclerosis. Mediators Inflamm 2013:659282.

Lund SA, Wilson CL, Raines EW, Tang J, Giachelli CM, Scatena M (2013) Osteopontin mediates macrophage chemotaxis via alpha4 and alpha9 integrins and survival via the alpha4 integrin. J Cell Biochem 114:1194-1202.

Malik AF, Hoque R, Ouyang X, Ghani A, Hong E, Khan K, Moore LB, Ng G, Munro F, Flavell RA, Shi Y, Kyriakides TR, Mehal WZ (2011) Inflammasome components Asc and caspase-1 mediate biomaterial-induced inflammation and foreign body response. Proc Natl Acad Sci U S A 108:20095-20100.

Matsui Y, Rittling SR, Okamoto H, Inobe M, Jia N, Shimizu T, Akino M, Sugawara T, Morimoto J, Kimura C, Kon S, Denhardt D, Kitabatake A, Uede T (2003) Osteopontin deficiency attenuates atherosclerosis in female apolipoprotein E-deficient mice. Arterioscler Thromb Vasc Biol 23:1029-1034.

McNally AK, Macewan SR, Anderson JM (2008) Foreign body-type multinucleated giant cell formation requires protein kinase C beta, delta, and zeta. Exp Mol Pathol 84:37-45.

Meller R, Stevens SL, Minami M, Cameron JA, King S, Rosenzweig H, Doyle K, Lessov NS, Simon RP, Stenzel-Poore MP (2005) Neuroprotection by osteopontin in stroke. J Cereb Blood Flow Metab 25:217-225.

Mi Z, Oliver T, Guo H, Gao C, Kuo PC (2007) Thrombin-cleaved COOH(-) terminal osteopontin peptide binds with cyclophilin C to CD147 in murine breast cancer cells. Cancer Res 67:4088-4097.

Miklossy J, Van der Loos H (1987) Cholesterol ester crystals in polarized light show pathways in the human brain. Brain research 426:377-380.

Miklossy J, Clarke S, Van der Loos H (1991) The long distance effects of brain lesions: visualization of axonal pathways and their terminations in the human brain by the Nauta method. Journal of neuropathology and experimental neurology 50:595-614.

Moore KJ, Sheedy FJ, Fisher EA (2013) Macrophages in atherosclerosis: a dynamic balance. Nature reviews Immunology 13:709-721.

Mroczko B, Groblewska M, Barcikowska M (2013) The role of matrix metalloproteinases and tissue inhibitors of metalloproteinases in the pathophysiology of neurodegeneration: a literature study. J Alzheimers Dis 37:273-283.

Nguyen TV, Frye JB, Zbesko JC, Stepanovic K, Hayes M, Urzua A, Serrano G, Beach TG, Doyle KP (2016) Multiplex immunoassay characterization and species comparison of inflammation in acute and non-acute ischemic infarcts in human and mouse brain tissue. Acta Neuropathol Commun 4:100.

Oh Y, Oh I, Morimoto J, Uede T, Morimoto A (2014) Osteopontin has a crucial role in osteoclast-like multinucleated giant cell formation. J Cell Biochem 115:585-595.

Orth M, Bellosta S (2012) Cholesterol: its regulation and role in central nervous system disorders. Cholesterol 2012:292598.

Park YM (2014) CD36, a scavenger receptor implicated in atherosclerosis. Exp Mol Med 46:e99.

Poli G, Biasi F, Leonarduzzi G (2013) Oxysterols in the pathogenesis of major chronic diseases. Redox Biol 1:125-130.

Pollak J, Doyle KP, Mamer L, Shamloo M, Buckwalter MS (2012) Stratification substantially reduces behavioral variability in the hypoxic-ischemic stroke model. Brain Behav 2:698-706.

Ramji DP, Davies TS (2015) Cytokines in atherosclerosis: Key players in all stages of disease and promising therapeutic targets. Cytokine Growth Factor Rev 26:673-685.

Robbins SL, Kumar V, Cotran RS (2010) Robbins and Cotran pathologic basis of disease, 8th Edition. Philadelphia, PA: Saunders/Elsevier.

Scatena M, Liaw L, Giachelli CM (2007) Osteopontin: a multifunctional molecule regulating chronic inflammation and vascular disease. Arterioscler Thromb Vasc Biol 27:2302-2309.

Schmitt S, Castelvetri LC, Simons M (2015) Metabolism and functions of lipids in myelin. Biochimica et biophysica acta 1851:999-1005.

Sheikh Z, Brooks PJ, Barzilay O, Fine N, Glogauer M (2015) Macrophages, Foreign Body Giant Cells and Their Response to Implantable Biomaterials. Materials (Basel) 8:5671-5701.

Stewart CR, Stuart LM, Wilkinson K, van Gils JM, Deng J, Halle A, Rayner KJ, Boyer L, Zhong R, Frazier WA, Lacy-Hulbert A, El Khoury J, Golenbock DT, Moore KJ (2010) CD36 ligands promote sterile inflammation through assembly of a Toll-like receptor 4 and 6 heterodimer. Nat Immunol 11:155-161.

Tangirala RK, Jerome WG, Jones NL, Small DM, Johnson WJ, Glick JM, Mahlberg FH, Rothblat GH (1994) Formation of cholesterol monohydrate crystals in macrophage-derived foam cells. J Lipid Res 35:93-104.

Watanabe N, Ikeda U (2004) Matrix metalloproteinases and atherosclerosis. Curr Atheroscler Rep 6:112-120.

Yamaguchi R, Hosaka M, Torii S, Hou N, Saito N, Yoshimoto Y, Imai H, Takeuchi T (2011) Cyclophilin C-associated protein regulation of phagocytic functions via NFAT activation in macrophages. Brain research 1397:55-65.

Zbesko JC, Nguyen TV, Yang T, Frye JB, Hussain O, Hayes M, Chung A, Anthony Day W, Stepanovic K, Krumberger M, Mona J, Longo FM, Doyle KP (2018) Glial scars are permeable to the neurotoxic environment of chronic stroke infarcts. Neurobiol Dis.

Zhang K, McQuibban GA, Silva C, Butler GS, Johnston JB, Holden J, Clark-Lewis I, Overall CM, Power C (2003) HIV-induced metalloproteinase processing of the chemokine stromal cell derived factor-1 causes neurodegeneration. Nat Neurosci 6:1064-1071.

Zhu Y, Lyapichev K, Lee DH, Motti D, Ferraro NM, Zhang Y, Yahn S, Soderblom C, Zha J, Bethea JR, Spiller KL, Lemmon VP, Lee JK (2017) Macrophage Transcriptional Profile Identifies Lipid Catabolic Pathways That Can Be Therapeutically Targeted after Spinal Cord Injury. J Neurosci 37:2362-2376.